Laser and Fourier-transform spectroscopy of KCa

Julia Gerschmann,[1,2,*] Erik Schwanke,[1,2,†] Asen Pashov,[3] Horst Knöckel,[1,2] Silke Ospelkaus,[1,2] and Eberhard Tiemann[1,2]

[1]*Institute of Quantum Optics, Leibniz Universität Hannover, Welfengarten 1, 30167 Hannover, Germany*

[2]*Laboratory for Nano- and Quantum Engineering, Leibniz Universität Hannover, Schneiderberg 39, 30167 Hannover, Germany*

[3]*Department of Physics, Sofia University, 5 James Bourchier Boulevard, 1164 Sofia, Bulgaria*

(Received 27 July 2017; published 6 September 2017)

KCa was produced in a heat-pipe oven and its thermal emission spectrum around 8900 cm^{-1} was recorded with a high-resolution Fourier-transform spectrometer. In addition, many selected transitions of this spectrum between deeply bound vibrational levels of the $X(1)^2\Sigma^+$ and $(2)^2\Sigma^+$ states were studied using laser excitation to facilitate the assignment of the lines. The ground state is described for $v'' = 0$–5 and the $(2)^2\Sigma^+$ state for $v' = 0-8$ with rotational levels up to 175. For both states, Dunham coefficients, spin-rotation parameters, and potential energy curves are derived.

DOI: 10.1103/PhysRevA.96.032505

I. INTRODUCTION

Molecules consisting of one alkali-metal atom and one alkaline-earth-metal atom are receiving increasing interest because of their prospective application in the field of ultracold quantum gases, as their ground state $X(1)^2\Sigma^+$, with its electric and magnetic dipole moments, offers advantageous properties (see, e.g., Refs. [1–3]) for testing and/or demonstrating fundamental properties of quantum gases. After investigating LiCa [4] and LiSr [5], we proceeded to the heavier KCa for opening perspectives for spectroscopic studies of even heavier species like RbSr, for which ultracold ensembles of Rb and Sr have already been prepared [2]. Compared to LiCa and LiSr, however, the experimental study of KCa becomes more difficult because of the higher density of spectral lines of KCa and the always accompanying molecule K_2. We present a spectroscopic observation of KCa and its first rovibrational analysis, from which the bottoms of the potential energy curves of the ground state $X(1)^2\Sigma^+$ and the first excited state $(2)^2\Sigma^+$ are derived.

Ab initio calculations for KCa have been performed by other groups [6,7]. Figure 1 shows a part of the potential energy scheme of KCa for the lowest atom pair asymptote $K(4s\,^2S) + Ca(4s^2\,^1S)$ and the excited asymptotes $K(4p\,^2P) + Ca(4s^2\,^1S)$ and $K(4s\,^2S) + Ca(4s4p\,^3P)$.

We started by recording the thermal emission spectrum of KCa in a heat pipe to locate the general position of the spectrum and to discriminate it from the K_2 spectrum. The observed spectrum was found in the near-infrared region, expected from the *ab initio* results shown in Fig. 1. Laser excitations of the molecule were performed and were essential for unambiguous assignment of the dense and overlapping spectral structure. Methods to interpret the results of such experiments for gathering structural information about the molecule are described. For the observed $(2)^2\Sigma^+$-$X(1)^2\Sigma^+$ system, molecular parameters are derived. A comparison of results from *ab initio* studies with experimental findings of this work is presented.

II. EXPERIMENT

The spectroscopic setup consists of a heat-pipe oven for the molecular gas and an optical system for imaging the thermal emission spectrum into a Fourier-transform spectrometer (FTS). The heat pipe is shown in Fig. 2. It is an 88-cm-long steel tube with a diameter of 3 cm. The middle section of the heat pipe is enclosed by an oven. The ends of the heat pipe are cooled to room temperature via water-cooling so that no metal vapor can reach the BK7 windows. The windows are tilted to avoid back reflections. The outer regions of the heat pipe are internally covered with a steel mesh approximately 30 cm in length, so that the condensed metal can flow back into the heated middle section. Additionally, shells cooled with forced airflow are installed in these regions (see Fig. 2) to create lower temperature areas and an appropriate temperature gradient for the very different vapor pressures of Ca and K. During the experimental run, crystals grow inside the heat pipe, producing laser stray light and, finally, blocking the optical path. This significantly reduces the measuring time, to about 5 h. Therefore, they must be melted intermittently by changing the heat-pipe position in the oven. The use of cooling shells slows crystal growth.

To prepare the heat pipe, 10 g of calcium is placed in the middle of the heat pipe and melted under an atmosphere of 200–300 mbar of argon at an oven temperature of up to 1000 °C. After the heat pipe is cooled down, 5 g of potassium is placed on the mesh at a distance of about 25 cm from calcium in the outer region of the heat pipe not facing the spectrometer. Potassium is melted at the same buffer gas pressure as for melting calcium and an oven temperature of 400 °C. Afterwards, the cooling shells are installed.

The light emerging from the heat pipe is imaged into the FTS (IFS 120HR; Bruker) via a mirror and a lens system and, finally, detected by an IR-enhanced silicon avalanche photodiode (S11519-30; Hamamatsu). The laser light is introduced counter-propagating the imaging path of the thermal emission to avoid direct laser radiation into the FTS. For this purpose, the mirror is slit and the laser beam propagates along the optical axis within the heat pipe, indicated in Fig. 2.

To produce KCa molecules, the region of the heat pipe at the calcium position is heated to approximately 820 °C. By varying the airflow, the cooling shells create a region

*gerschmann@iqo.uni-hannover.de
†schwanke@iqo.uni-hannover.de

 ©2017 American Physical Society

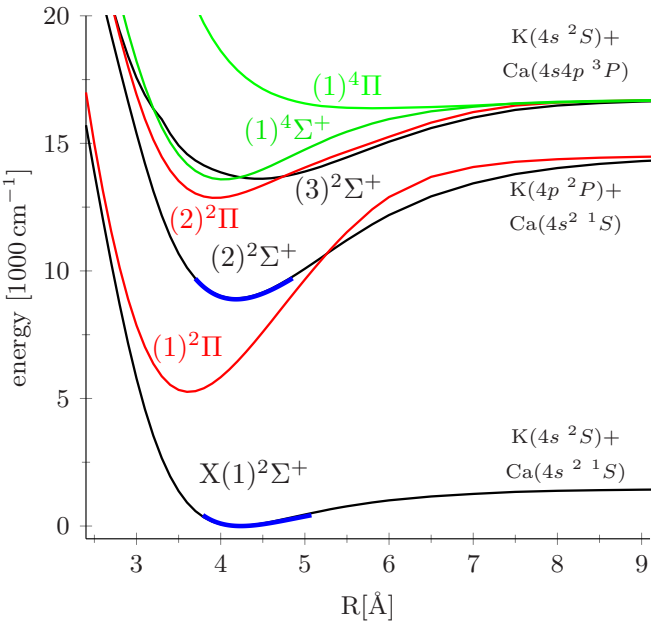

FIG. 1. Potential energy curves of KCa from *ab initio* calculations [7]. Thick curves represent PECs derived from the experimental data of this work.

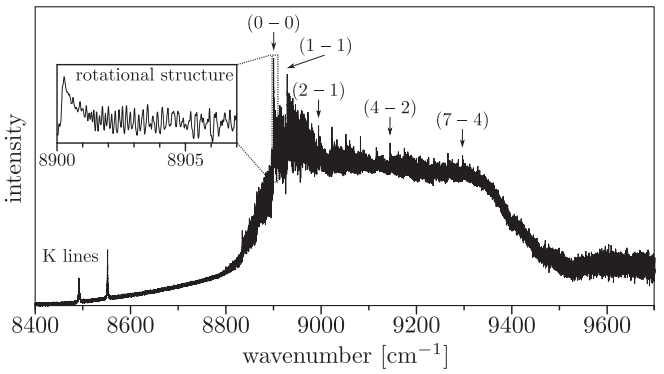

FIG. 3. Record of the thermal emission of KCa. Inset: Rotational structure shown enlarged. Some band heads of the vibrational structure are labeled.

of 260°–340 °C on the side of the potassium and a region of 450°–650 °C on the other side. During measurements, the pressure of the buffer gas, argon, is about 50 mbar.

In addition to KCa, K_2 molecules form in the heat pipe even at low temperatures and dominate the gas spectrum. Since the observed emission lines of both molecules lie in different spectral ranges, this does not affect the observation of KCa. We use K_2 to align the imaging of the fluorescence region by exciting K_2 molecules with a HeNe laser and adjusting the mirror so that only the fluorescence, and no stray light from the walls, is recorded.

The thermal emission is observed in the range from 8000 to 9700 cm^{-1}. Figure 3 shows the spectrum recorded with a resolution of 0.03 cm^{-1} and represents an average of 290 scans. On the left, one can clearly see lines at 8491.8 and 8551.8 cm^{-1}, which correspond to the atomic potassium transitions $^2P_{3/2}$-$^2D_{5/2}$ and $^2P_{1/2}$-$^2D_{3/2}$. The KCa spectrum of the $(2)^2\Sigma^+$-$X(1)^2\Sigma^+$ band is located between 8800 and 9400 cm^{-1}, as expected from the *ab initio* calculations [7]. The shape of the background in this area changes with the temperature in the heat pipe. Since the conditions in the heat pipe change over time, the recordings have different background shapes, but this does not influence the position of the lines.

One can well recognize band heads, the largest of which is at 8900.3 cm^{-1} and is assigned to the (0-0) band on the basis of Franck-Condon factors (FCFs) derived from the *ab initio* potentials. The inset in Fig. 3 is a zoom-in showing the rotational structure clearly.

Due to the atomic masses of about 40 u and the fairly shallow ground-state potential, the rotational and vibrational constants of KCa are rather small. Furthermore, the high temperature needed to produce the molecules leads to a wide range of populated vibrational and rotational levels, and due to the FCFs thermal emission is distributed over many vibrational transitions. The vibrational bands are strongly overlapping, which hinders direct assignment. Therefore, laser-induced fluorescence (LIF) is used to identify pairs of lines according to the selection rule $\Delta J = \pm 1$ for the common total angular momentum of the excited state, J', and associate lines of a vibrational progression within the ground state.

To excite the KCa molecules, a tunable diode laser with an antireflection coating (Toptica) is used in a Littrow configuration, and it is stabilized by a wavemeter (WS-U; HighFinesse GmbH), leading to an uncertainty of the exciting laser frequency of less than 20 MHz. The frequency range of the diode is about 8730–9350 cm^{-1}. The laser light, with a power of 10–20 mW and a beam diameter of approximately 2 mm is precisely adjusted along the optical axis, which is fixed beforehand by the fluorescence observation of K_2 induced by a HeNe laser. Lines selected from the emission spectrum are excited and the fluorescence spectra are recorded with a resolution of 0.05 cm^{-1}. The fluorescence progression appears as enhanced lines in the thermal emission. An overview of the fluorescence studies is given in Table I(a).

Because a recorded spectral line consists of several overlapping Doppler-broadened transitions, we assign an uncertainty of 0.02 cm^{-1} to most transition frequencies. For broad lines, a higher uncertainty is assumed. The measured frequency differences have generally been given an uncertainty of 0.01 cm^{-1} if the fluorescence lines are sufficiently enhanced compared to the thermal emission spectrum because of the

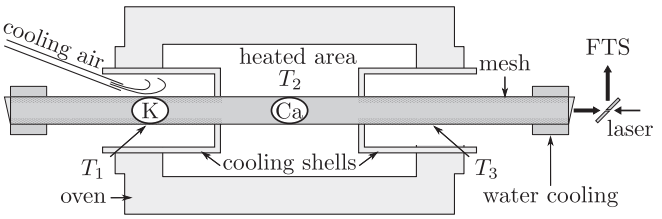

FIG. 2. Experimental setup of the heat pipe. The heat pipe is driven by an oven. Three temperature ranges are created by cooling shells: T_1, 260°–340 °C; T_2, 820 °C; and T_3, 450°–650 °C.

TABLE I. (a) Ranges of N levels observed in each band via LIF experiments. (b) Ranges of all assigned N levels.

(a)					(b)									
v''	$v'=0$	$v'=1$	$v'=2$	$v'=3$	v''	$v'=0$	$v'=1$	$v'=2$	$v'=3$	$v'=4$	$v'=5$	$v'=6$	$v'=7$	$v'=8$
0	8–162	46–145			0	8–174	46–176	119–175	146–171					
1	4–162	14–123	9–132	62–93	1	4–162	14–123	9–150	62–160	125–144				
2	131–155	34–143	9–68	62–93	2	131–155	34–143	9–68	39–103	44–147	49–149	115–147		
3		84–145	9–103		3		84–146	9–110		47–80	32–108	48–133		
4			54–123	62–93	4		137–154	21–123	62–93			19–79	41–85	
5			119–132	62–93	5			119–132	47–93		77–84			39–89

significantly reduced Doppler shift due to mismatch of the laser excitation.

III. ANALYSIS

A. Overview

Laser excitations in the band heads yield easily recognizable fluorescence (by the enhanced intensity compared to the primary thermal emission) in other band heads which can be used to order the vibrational structure of the $X(1)^2\Sigma^+$ and $(2)^2\Sigma^+$ states. Figures 4(a) to 4(c) show eight vibrational bands which are associated in three systems of almost-equal vibrational spacing, representing the vibration of the ground state. The laser excitation is at the overshooting line. The short progressions also allowed for a preliminary assignment of vibrational quantum numbers starting with $v''=0$, since no fluorescence could be observed beyond this labeled line. This assignment is consistent with the FCFs calculated later (see Sec. V). In Fig. 4, the three progressions are aligned vertically on the same absolute scale. The vibrational ladder for the excited state becomes visible as differences between two such recordings as indicated in Fig. 4(d). The obtained vibrational spacings allowed for extrapolation of the vibrational ladders. The band heads predicted in this way coincide with other band heads observed up to (7-4) in the thermal emission spectrum, even if they showed no or hardly recognizable fluorescence, as indicated in Fig. 3.

The bands are blue shaded, thus the band head is given by the P branch. Excitations in the band heads could yield fluorescence of a group of rotational lines in the R branch as shown in Fig. 4(a) above the band head (0-0). These rotational fluorescences form two distinct systems, later identified as transitions between spin-up states and spin-down states, labeled F_1 and F_2 (see Sec. III B). Figure 5 depicts these fluorescences in detail, explaining the appearance of the group

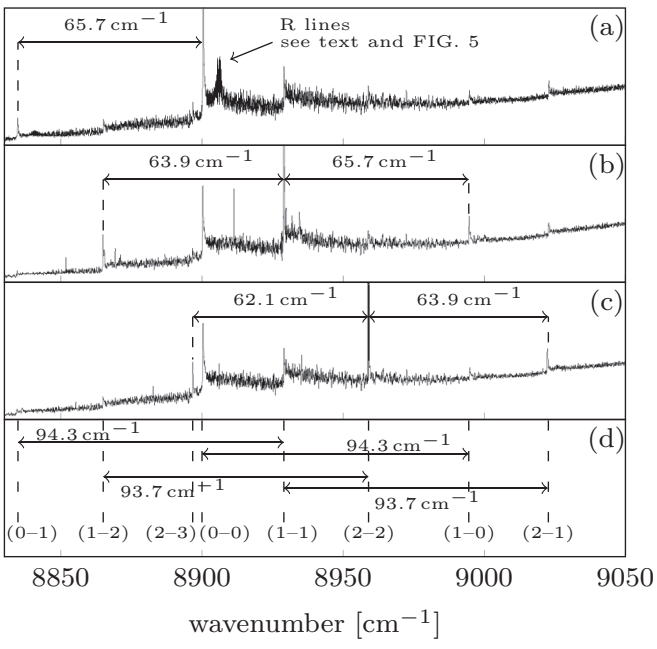

FIG. 4. (a–c) Exemplary LIF spectra with excitations of different band heads show three linked systems of bands. Identifying equal distances between these bands allows connection of these systems to a coherent structure of vibrational levels in the ground state. (d) Selecting identical v'' gives the vibrational levels in the excited state.

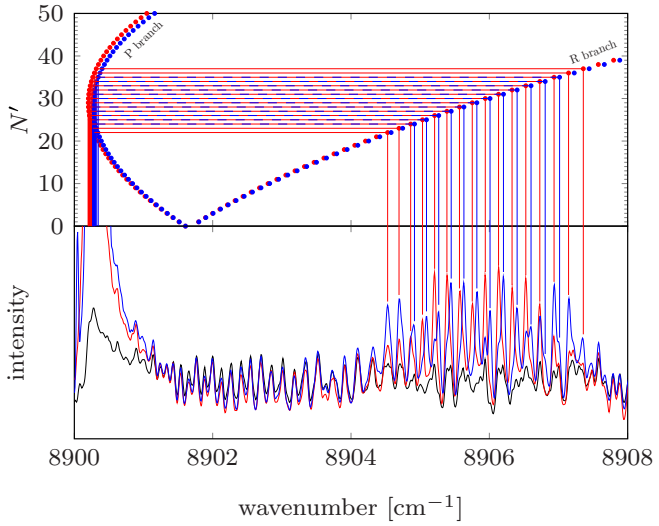

FIG. 5. Red and blue spectra show LIF from excitations in the P band head of the (0-0) band of KCa and fluorescence lines in the R branch. The black thermal emission spectrum is shown for reference. The upper part of the figure shows the Fortrat parabolas corresponding to the P and R branches for N' separating the overlaps in the band head to the wide spread in the R branch. Red and blue circles correspond to F_1 and F_2 levels, respectively. The two cases of excitations show the differences between F_1 and F_2: the red spectrum contains only florescence of F_1 lines; the blue spectrum contains mainly fluorescence of F_2 lines, with some F_1 lines at the edges of the fluorescence region.

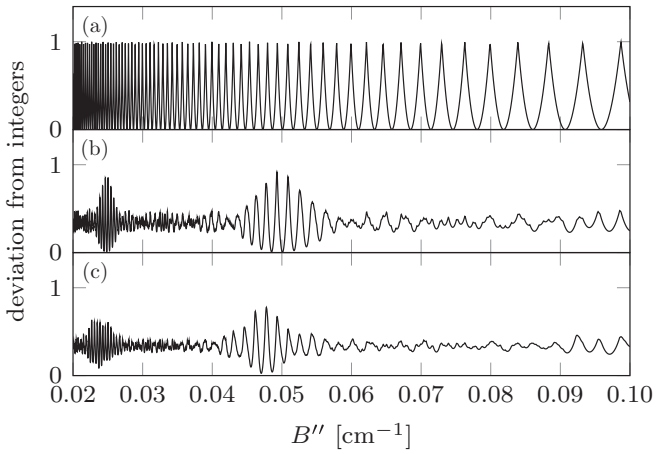

FIG. 6. Accumulated deviation from integer numbers for N' for (a) 1 $\Delta\nu$ measurement, (b) 6 $\Delta\nu$ measurements, and (c) 11 $\Delta\nu$ measurements from a LIF experiment in the (0-0) band head. Note that in (b) the global minimum does not yet give the correct value. For more than 11 values, the general shape of the curve is not altered.

of rotational lines and the possibility of observing the energy difference between the F_1 and the F_2 lines by only slightly shifting the excitation frequency in the band head. We should point out that the experiment does not give information on which line system is F_1 or F_2. Similar groups of fluorescence lines were also observed for the (0-1) band.

The lines of such a group correspond to consecutive rotational quantum numbers N. [We use N as the rotational quantum number; see later Hund's coupling case (b)]. For relatively small ranges of N, the changes in the effective rotational constant B are negligible, thus the frequency differences $\Delta\nu$ of the PR pairs for N' follow the formula

$$\Delta\nu = B''(4N' + 2). \tag{1}$$

Requiring that N' is an integer, a discrete set of values for the rotational constant is derived from each observed $\Delta\nu$. For several observed PR differences, we construct the sum over the weighted quadratic distances to the closest integer for each observation with index i,

$$\frac{1}{\#_{\text{obs}}} \sum_i \left(\frac{N_i'(B) - \mathcal{N}_i'(B)}{\delta\nu_i} 2\,\delta\nu_{\min} \right)^2, \tag{2}$$

and the minimum of this function with respect to B gives the value for B'' of the studied band. Here, $\#_{\text{obs}}$ is the number of observations, $\mathcal{N}_i'(B)$ is calculated with the observed $\Delta\nu_i$ from rearranging Eq. (1), $N_i'(B)$ is the integer closest to $\mathcal{N}_i'$, $\delta\nu_i$ is the experimental uncertainty of $\Delta\nu_i$, and the factor $2\delta\nu_{\min}$, with the smallest uncertainty in the series, serves to normalize the expression. Figure 6 exemplifies such sums in dependence of a given rotational constant B''. Figure 6(a) is the example of a single observation and the zero positions represent the discrete set of possible B'' values mentioned above. Adding more and more observations [from Fig. 6(b) to Fig. 6(c)], the desired minimum of the function becomes more pronounced. The value for B'' determined with this procedure from Fig. 6(c) is 0.0470 cm^{-1} and close to the later determined value of Y''_{01} of the full evaluation (see Table II).

B'' having thus been determined, Eq. (1) could directly be applied to assign rotational quantum numbers to the observed fluorescence lines and the fluorescence lines in other vibrational bands from the same LIF spectrum. These assignments together with B'' can immediately be used to determine a value for B'. Thus LIF experiments with the laser tuned to several band heads provided the starting point for the analysis of the rovibrational spectrum.

B. Assignment and molecular parameters

Hund's coupling case (b) with the basis vector $|\Lambda,(N,S)J\rangle$ is used to describe both $^2\Sigma^+$ states, where Λ is the quantum number associated with the projection of the orbital angular momentum to the molecular axis (here $\Lambda = 0$), $\hat{N}$ is the total angular momentum without spins, $\hat{S}$ is the total spin of the electrons, and $\hat{J} = \hat{N} + \hat{S}$ is the total angular momentum of the molecule excluding the nuclear spins. The rovibrational energies can be expressed by the Dunham expansion

$$E(v,N) = \sum_{m,n} \mathrm{Y}_{mn} \left(v + \frac{1}{2} \right)^m [N(N+1)]^n, \tag{3}$$

TABLE II. Dunham and spin-rotation parameters for the first two $^2\Sigma^+$ states of ^{39}K^{40}Ca. The parameters give an accurate description for levels with quantum numbers as listed in Table I. All values given in cm^{-1}.

n	Y_{n0}	Y_{n1}	Y_{n2}	Y_{n3}	Y_{n4}
			$X(1)^2\Sigma^+$		
0	0.0	$4.75384(25) \times 10^{-2}$	$-9.3968(190) \times 10^{-8}$	$-8.54(88) \times 10^{-14}$	$-6.57(15) \times 10^{-18}$
1	67.9826(37)	$-6.4306(84) \times 10^{-4}$	$-2.062(64) \times 10^{-9}$	$-7.20(14) \times 10^{-14}$	—
2	$-9.3950(45)10^{-1}$	$-5.87(15) \times 10^{-6}$	$-1.771(74) \times 10^{-10}$	—	—
3	$-1.01(15) \times 10^{-3}$	—	—	—	—
γ_{10}	$2.05(66) \times 10^{-5}$				
			$(2)^2\Sigma^+$		
0	8888.0459(36)	$4.88331(22) \times 10^{-2}$	$-5.0278(75) \times 10^{-8}$		
1	94.9595(29)	$-1.9686(31) \times 10^{-4}$	$-1.446(89) \times 10^{-10}$		
2	$-2.7120(85) \times 10^{-1}$	$-1.049(31) \times 10^{-6}$			
3	$-1.636(74) \times 10^{-3}$	—	—		
γ_{00}[a]	$-2.234(14) \times 10^{-3}$				

[a]Note that the experimental data only yield the difference, namely, $\gamma'_{00} - \gamma''_{00}$.

for each electronic state with the so-called Dunham parameters Y_{mn}. The parameter Y_{00} is used in this analysis to approximate the electronic term energy T_e and thus has a different meaning than the conventional Dunham correction Y_{00}.

The energy levels with $J = N + 1/2$ and $J = N - 1/2$ of a doublet state ($S = 1/2$) are labeled F_1 and F_2, respectively, and are split for the same N because of the spin-rotation coupling given by the Hamiltonian $\gamma \hat{S} \cdot \hat{N}$ with the coupling constant γ [8]. This energy is added to the rovibrational energies since the interaction operator is diagonal in the Hund's case (b) basis:

$$E = E(v,N) + \frac{\gamma}{2} \times N \qquad \text{for } F_1, \tag{4a}$$

$$E = E(v,N) - \frac{\gamma}{2} \times (N+1) \qquad \text{for } F_2. \tag{4b}$$

In principle, the spin-rotation contribution will depend on the vibrational and rotational level and thus could be described by a corresponding Dunham-like series with γ_{mn} as expansion parameters. Our evaluation program contains this form for both states, but the energy expression being linear in N results for P and R transitions to a function which mainly depends on the differences in the spin-rotation interactions of the two electronic states. Thus we choose γ_{00} of the excited state as nonzero and this value actually represents the difference between the two interactions. Because we have sets of fluorescence progressions, each with a common excited level, we found that the data contain a slight γ dependence of the vibrational level of the ground state, thus we introduced for this fact the parameter γ_{10} for the ground state. All other expansion parameters γ_{mn} were set to 0.

The parameters Y_{00}, Y_{01} for both states and γ_{00} of the excited state can be fitted using the fluorescence spectra of the (0-0) band-head excitations. Starting with these initial parameters, more fluorescence lines with assigned quantum numbers are subsequently included in the fit based on their PR differences. Similarly, fluorescence lines from other vibrational bands are included.

Since the KCa spectrum is dense, the laser we use in an LIF experiment can affect several transitions from different bands. Examples of such cases of fluorescence are shown in Fig. 7. In this figure, two laser excitations are shown on the same absolute scale to illustrate the relation of the different vibrational bands. In both cases, two progressions are excited simultaneously. Figure 7(b) shows very different N's and results in Stokes pairs of band (0-1) and Fig. 7(a) is an excitation of a line in (0-0) and one in (0-1) showing anti-Stokes fluorescence to (0-0). From the fluorescence spectra, lines from bands with $v' = 0$–2 and $v'' = 0$–3 could initially be identified and assigned. Reviewing the fluorescence spectra with the final molecular parameters yielded the identification of additional fluorescence lines with $v' = 3$ and $v'' = 4$–5. The ranges of observed rotational quantum numbers are listed in Table I.

Further bands are analyzed using the thermal emission spectrum. For this purpose, the thermal emission spectrum is simulated with the Dunham parameters determined up to the actual intermediate evaluation step with FCFs derived from the initial *ab initio* potentials and a line width estimated from

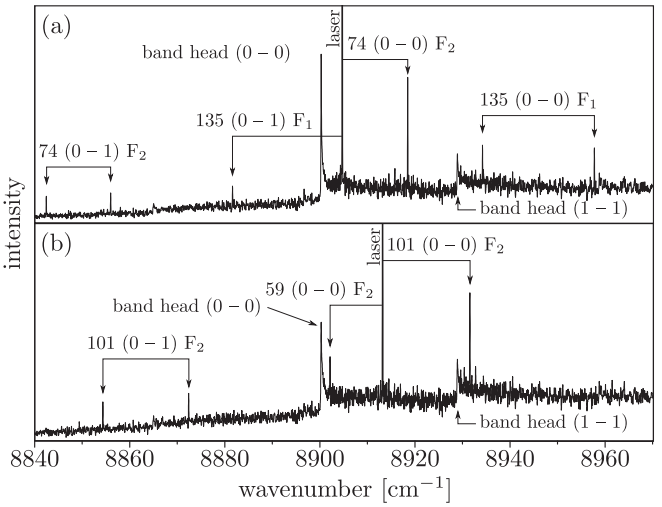

FIG. 7. Laser-induced fluorescence of two excitations, at (a) 8904.7115 cm^{-1} and (b) 8913.2055 cm^{-1}. P-R pairs are labeled with the rotational quantum number N' of the excited state, the vibrational band, and the component of the spin-rotation coupling.

the Doppler width and the selected resolution of the FTS and a population according to the actual temperature. This theoretical spectrum is compared with the recorded spectrum and allows for adding additional lines to the fit and to adjust the parameters and add new ones. Occasionally, the simulated spectrum shows a high-intensity line close to lines of similar intensity and width in the experimentally recorded spectrum. If these lines show this behavior for a long series of quantum numbers, they are identified with the lines from the recorded spectrum and a fit will show the consistency with the other assignments done before. The extension in quantum number space was done in small steps, avoiding large extrapolation in quantum numbers v and N, because due to the dense spectra assigning a wrong line is very probable. If this is done carefully, the shape of the simulated spectrum converges to the shape of the experimental spectrum.

In total, 2554 lines and frequency differences could be measured between 878 levels in the ground state up to $v'' = 5$ and 549 levels in the excited state up to $v' = 8$. The resulting Dunham parameters are listed in Table II with their estimated standard deviations. The normalized standard deviation $\sigma = 0.95$ of this linear fit validates the choice of the uncertainties described in Sec. II. All assigned lines used in the the final fit of the Dunham parameters are reported in the Supplemental Material [9].

IV. POTENTIAL FIT

The evaluation with the Dunham expansion shows that the two electronic states are well described by Hund's coupling case (b) with basis vectors $|\Lambda,(N,S)J\rangle$ and possible coupling to other electronic states, for example, by spin-orbit coupling is not observed within the present experimental accuracy of 0.02 cm^{-1}. Thus we can set up two separate Hamiltonians for the two states. Because the spin-rotation interaction is diagonal in the basis, the corresponding energy contribution adds to the rovibrational eigenenergies $E(v,N)$ as given in Eq. (4).

The Schrödinger equation for the rovibrational energies and for the rovibrational wave function ψ_{vN} has the conventional form

$$\left[-\frac{\hbar^2}{2m}\frac{\mathrm{d}^2}{\mathrm{d}R^2}+U(R)+\frac{\hbar^2}{2mR^2}N(N+1)\right]\psi_{vN}(R) = E(v,N)\psi_{vN}(R), \quad (5)$$

with the reduced mass m of the molecule and the potential function $U(R)$ for each electronic state. The potential function approach gives the advantage of releasing the constraints by truncation of the power expansion in quantum numbers (v,N) for the energies in the Dunham representation. Such a possible effect can be contained in the solution in Table II looking at the different centrifugal contributions for the two electronic states, namely, the highest term for the excited state, Y_{02}, and for the ground state, Y_{04}.

For solving the Schrödinger equation, we set up the potential in analytic form as successfully applied in several earlier papers (e.g., [10]),

$$U(R)=\sum_{i=0}^{n} a_i\,\xi(R)^i, \quad (6)$$

$$\xi(R)=\frac{R-R_m}{R+b\,R_m}, \quad (7)$$

where the coefficients a_i are fitted parameters and b and R_m are fixed. R_m is normally set close to the value of the equilibrium separation R_e. The potential is extrapolated for $R < R_{\mathrm{inn}}$ with

$$U(R)=A+B/R^{N_s} \quad (8)$$

by adjusting the parameters A, B with $N_s=6$ to get a continuous transition at R_{inn}. For large internuclear separations $(R > R_{\mathrm{out}})$ we adopted the standard long-range form:

$$U_{\mathrm{LR}}=U_\infty-C_6/R^6-C_8/R^8-C_{10}/R^{10}. \quad (9)$$

The dispersion parameters C_i do not play any role in our present case, because we observed only low vibrational levels and did not reach the long-range region in R, thus these parameters serve to set up a smooth potential function to the dissociation limit U_∞.

A nonlinear least-squares fit to all assigned transitions and transition differences with common upper levels obtained from the fluorescence study was performed, fitting the potential functions for the two electronic states simultaneously. The spin-rotation contribution was included in exactly the same form as used before; see Eq. (4). The fit describes the experimental data with the same quality, namely, the normalized standard deviation $\sigma=0.94$, as obtained for the Dunham fit. The derived potential parameters are listed in Tables III and IV, the number of fit parameters is only 20, thus lower than that in the Dunham case, (i.e., 22), which demonstrates the compact form of the representation by potentials. If one looks closely at the individual deviations between the Dunham and the potential approach, one sees differences mainly for high rotational levels N, which certainly is related to the above-mentioned constraint by the truncation in the Dunham model. On average the deviations of both approaches are the same. An example of the systematic trend with quantum number N between the two approaches is included in the Supplemental Material [9].

TABLE III. Parameters of the analytic representation of the potential for state $X(1)^2\Sigma^+$. Parameters followed by a superscript asterisk ensure smooth continuous extrapolation of the potential at R_{inn} and R_{out}. U_∞ is used to construct the dissociation asymptote.

$R < R_{\mathrm{inn}} = 3.72$ Å	
A^*	$-0.17137691 \times 10^4\ \mathrm{cm}^{-1}$
B^*	$0.623058968 \times 10^7\ \mathrm{cm}^{-1}\ \text{Å}^6$
$R_{\mathrm{inn}} \leqslant R \leqslant R_{\mathrm{out}} = 5.3$ Å	
b	-0.50
R_{m}	4.23968785 Å
a_0	$0.000010\ \mathrm{cm}^{-1}$
a_1	$0.916715672820951011\ \mathrm{cm}^{-1}$
a_2	$0.607228674244838840 \times 10^4\ \mathrm{cm}^{-1}$
a_3	$-0.661911115663710007 \times 10^3\ \mathrm{cm}^{-1}$
a_4	$-0.610926466028853429 \times 10^4\ \mathrm{cm}^{-1}$
a_5	$-0.180355143531396743 \times 10^4\ \mathrm{cm}^{-1}$
a_6	$-0.262462209324614050 \times 10^5\ \mathrm{cm}^{-1}$
a_7	$0.942565374511957998 \times 10^4\ \mathrm{cm}^{-1}$
a_8	$0.360954584572881111 \times 10^6\ \mathrm{cm}^{-1}$
a_9	$-0.637614449251196464 \times 10^6\ \mathrm{cm}^{-1}$
$R_{\mathrm{out}} < R$	
U_∞	$1475.0\ \mathrm{cm}^{-1}$
C_6 [11]	$0.13508721 \times 10^8\ \mathrm{cm}^{-1}\ \text{Å}^6$
C_8^*	$0.11594031 \times 10^{10}\ \mathrm{cm}^{-1}\ \text{Å}^8$
C_{10}^*	$-0.27203341 \times 10^{11}\ \mathrm{cm}^{-1}\ \text{Å}^{10}$
For all R	
γ_{10}	$0.228 \times 10^{-4}\ \mathrm{cm}^{-1}$

The potential functions derived by the potential fit are overlaid in Fig. 1 by thick lines in the region where they are determined from the observations. The agreement looks nice, but the differences hidden by the thick lines are of the order of $100\ \mathrm{cm}^{-1}$.

The potentials are also used to extend iteratively the assignment of the emission spectra, comparing the simulation of the spectra constructed by energies and FCFs with the thermal emission. We also calculated the spectrum of the second most abundant isotope combination of KCa, namely, $^{41}\mathrm{K}^{40}\mathrm{Ca}$, with 6.5% natural abundance, by mass scaling. In several places, the intensity of such lines would be large enough for observation but the overlap with other lines is too strong to obtain an unambiguous assignment.

V. DISCUSSION AND OUTLOOK

The fluorescence lines in the laser-addressed region (8820–9050 cm^{-1}) are clearly visible up to $v'=2$ and $v''=3$. Systematic comparison of the recorded spectrum of the thermal emission with the simulation applying Dunham parameters or potentials yields the description up to $v'=8$ and $v''=5$. Overall, lines in the range 8820–9380 cm^{-1} are assigned. The FCFs generated with the potentials (Tables III and IV) show, for $N=0$ in the range $v'=0$–8 and $v''=0$–8, a structure similar in magnitude to that in the *ab initio* work in Ref. [7], thus their conclusion about creation of cold

TABLE IV. Parameters of the analytic representation of the potential for state $(2)^2\Sigma^+$. Parameters followed by a superscript asterisk ensure smooth continuous extrapolation of the potential at $R_{\rm inn}$ and $R_{\rm out}$. U_∞ is used to construct the dissociation asymptote.

$R < R_{\rm inn} = 3.605$ Å	
A^*	$0.67975020 \times 10^4\ {\rm cm}^{-1}$
B^*	$0.73133965 \times 10^7\ {\rm cm}^{-1}\ {\rm Å}^6$
$R_{\rm inn} \leqslant R \leqslant R_{\rm out} = 5.1$ Å	
b	-0.24
$R_{\rm m}$	4.18303794 Å
a_0	$8888.0195\ {\rm cm}^{-1}$
a_1	$8.97211680301065329\ {\rm cm}^{-1}$
a_2	$0.266368790864483090 \times 10^5\ {\rm cm}^{-1}$
a_3	$0.672648244268816416 \times 10^4\ {\rm cm}^{-1}$
a_4	$-0.112400340636989258 \times 10^5\ {\rm cm}^{-1}$
a_5	$-0.904918359031159489 \times 10^5\ {\rm cm}^{-1}$
a_6	$-0.360117376114208950 \times 10^6\ {\rm cm}^{-1}$
a_7	$0.296505843717056094 \times 10^7\ {\rm cm}^{-1}$
a_8	$0.530811059962429386 \times 10^7\ {\rm cm}^{-1}$
a_9	$-0.538588415900813341 \times 10^8\ {\rm cm}^{-1}$
$R_{\rm out} < R$	
U_∞	$14500.0\ {\rm cm}^{-1}$
C_6^*	$0.10 \times 10^8\ {\rm cm}^{-1}\ {\rm Å}^6$
C_8^*	$0.68834939 \times 10^{10}\ {\rm cm}^{-1}\ {\rm Å}^8$
C_{10}^*	$-0.13481830 \times 10^{12}\ {\rm cm}^{-1}\ {\rm Å}^{10}$
For all R	
γ_{00}[a]	$-0.0022317\ {\rm cm}^{-1}$

[a]Note that the experimental data only yield the difference, namely, $\gamma'_{00} - \gamma''_{00}$.

molecules remains valid. In addition, the FCFs show a strong rotational dependency. When N is increased to large values, the distribution of significant FCFs covers a larger interval of vibrational levels (see FCF tables in the Supplemental Material [9]).

The simulation of the thermal emission spectrum with the potentials from Tables III and IV reproduces the recorded spectrum in the range 8835–9340 $\rm cm^{-1}$ well. High consistency is found in the ranges 8900–8940 $\rm cm^{-1}$, dominated by the (0-0) and (1-1) bands; 9040–9085 $\rm cm^{-1}$, dominated by the (1-0), (2-1), and (3-2) bands; and 9120–9190 $\rm cm^{-1}$, dominated by the (2-0), (3-1), (4-2), and (5-3) bands. For these bands, we have many assigned lines [see Table I(b)]. The spectral range 8940–9010 $\rm cm^{-1}$ is less well described. This is mainly due to the fact that in this region lie lines of bands with $v'' = 6$–10 and good FCFs that were not taken into account in the potential fit. Due to the strong overlap of the bands, even small displacements of these lines by incomplete modeling strongly influence the overall intensity profile. The spectrum below 8820 $\rm cm^{-1}$ and beyond 9380 $\rm cm^{-1}$ cannot be analyzed convincingly because the intensity is too low (see Fig. 3). A screenshot from the simulation program is shown in Fig. 8. At the top the individual transition positions are indicated by colored vertical bars. Note that small deviations of the measured and simulated profiles appear throughout the diagram. They can mostly be supposed to result from the sum of many lines, each of which might deviate within the uncertainty

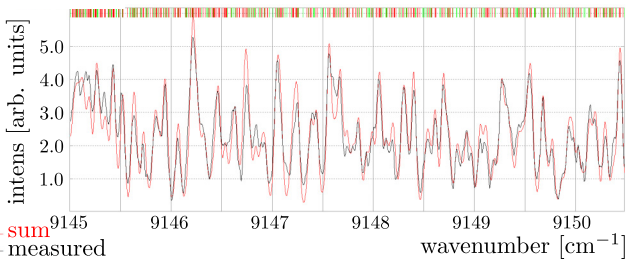

FIG. 8. Simulation of the spectrum in the region of 9145–9150.5 $\rm cm^{-1}$. The black curve represents the experimental spectrum; the red curve, the sum of the simulated spectra for the isotopologues ^{39}K^{40}Ca (90.4% natural abundance) and ^{41}K^{40}Ca (6.5% natural abundance). The red (^{39}K^{40}Ca) and green ^{41}K^{40}Ca bars at the top of the diagram represent calculated transitions for both isotopologues. For convenience, we have edited the text for better readability.

of the model from the "true" transition frequency; see the dense pattern at the top of the figure. Lines for the second most abundant isotopologue, ^{41}K^{40}Ca, are extrapolated since all transitions could be attributed to the main isotopologue, ^{39}K^{40}Ca.

With the help of the simulation, we revisited the fluorescence studies. The systematic inspection shows relatively long vibrational progressions with fluorescence intensities in agreement with the predicted FCFs. Many such fluorescence lines were not sufficiently pronounced compared to the thermal emission, so that they were overlooked in the former assignment process. This successful extension shows the overall consistency of the whole simulation despite the existence of less-well-described spectral regions mentioned above.

Both evaluation approaches, energy representation by Dunham coefficients and by molecular potentials, fit the measurement data equally well. Table V lists for comparison the molecular parameters determined in this work and those from known *ab initio* calculations. The agreement of the fitted parameters is very good and differences between Y_{10} defined by the Dunham approach and ω_e for the potentials are not significant, but they are different in definition and this is also true for Y_{01} and B_e. The experimentally determined equilibrium separation R_e and vibrational constant ω_e of the ground state lie between the two *ab initio* values. In the excited state, these theoretical values deviate from the experimental ones by less than 1%. The potential depth could not be derived because of missing high vibrational states. The experimentally determined electronic term energy of the excited state differs by only 34 $\rm cm^{-1}$ from the calculated value, confirming the good quality of the *ab initio* calculations.

Compared to the lighter molecule, LiCa [4], the rotational and spin rotational constants of KCa are smaller. KCa does not show any perturbations of the $2^2\Sigma^+$ state within the achieved accuracy, in contrast to LiSr, where we observed the coupling between $(2)^2\Sigma^+$ and $(1)^2\Pi$ in our previous work [5].

Because of the high density of the lines in the KCa emission spectrum, the LIF experiments were indispensable for assignment. To extend these results to higher vibrational bands, we will start a new series of laser excitations. We expect

TABLE V. Comparison of measured spectroscopic constants of $^{39}K^{40}Ca$ with results of known *ab initio* calculations. All values are given in cm^{-1}, except R_e, which is given in Å.

Method	R_e	D_e	$\omega_e \approx Y_{10}$	$\omega_e x_e \approx -Y_{20}$	$B_e \approx Y_{01}$	T_e	Ref. No.
			$X(1)^2\Sigma^+$				
CCSD(T)	4.32	974	61	—	0.045	0	[6]
MRCI	4.197	1474	70.8	0.85	—	0	[7]
Dunham	4.2377	—	67.983	0.940	0.047538	0	This work
Potential fit	4.2395	—	67.971	—	0.047541	0	This work
$(2)^2\Sigma^+$							
MRCI	4.177	5633	95.0	0.40	—	8922[a]	[7]
Dunham	4.1811	—	94.960	0.271	0.048831	8888.047	This work
Potential fit	4.1825	—	94.937	—	0.048846	8888.019	This work

[a]Derived from the potential given in private communications.

to detect lines up to $v'' = 10$ of the ground state because of sufficiently large FCFs. For further investigations of KCa, we will study $(3)^2\Sigma^+$-$X(1)^2\Sigma^+$ transitions in the visible spectral range for which a high transition dipole moment is predicted [7]. The relevant spectral region around $14\,000\,cm^{-1}$ should be sufficiently devoid of K_2 spectra [12], whereas Ca_2 lines can be expected [13] but should not dominate the spectrum. These proposed studies will provide higher vibrational levels of the ground state needed for extrapolating to the atom-pair asymptote, which is greatly desired for the study of ultracold KCa.

ACKNOWLEDGMENTS

We thank Alexander Stein for his contribution in the initial phase of this project. This work received financial support from 479 the Deutsche Forschungsgemeinschaft (DFG) (Grants No. TI 106/17-1 and No. OS 401/15-1).

[1] T. V. Tscherbul and R. V. Krems, Phys. Rev. Lett. **97**, 083201 (2006).
[2] B. Pasquiou, A. Bayerle, S. M. Tzanova, S. Stellmer, J. Szczepkowski, M. Parigger, R. Grimm, and F. Schreck, Phys. Rev. A **88**, 023601 (2013).
[3] R. Roy, R. Shrestha, A. Green, S. Gupta, M. Li, S. Kotochigova, A. Petrov, and C. H. Yuen, Phys. Rev. A **94**, 033413 (2016).
[4] A. Stein, M. Ivanova, A. Pashov, H. Knöckel, and E. Tiemann, J. Chem. Phys. **138**, 114306 (2013).
[5] E. Schwanke, H. Knöckel, A. Pashov, A. Stein, S. Ospelkaus, and E. Tiemann, submitted for publication (2017).
[6] G. Gopakumar, M. Abe, M. Hada, and M. Kajita, J. Chem. Phys. **140**, 224303 (2014).
[7] J. V. Pototschnig, R. Meyer, A. W. Hauser, and W. E. Ernst, Phys. Rev. A **95**, 022501 (2017).
[8] G. Herzberg, *Spectra of Diatomic Molecules I. Molecular Spectra and Molecular Structure* 2nd ed. (van Nostrand, New York, 1950).
[9] See Supplemental Material at http://link.aps.org/supplemental/10.1103/PhysRevA.96.032505 for the full recorded thermal emission spectrum, a list of the assigned lines used, an overview of the deviations of the Dunham and potential model, and derived tables of Franck-Condon factors for various N's.
[10] C. Samuelis, E. Tiesinga, T. Laue, M. Elbs, H. Knöckel, and E. Tiemann, Phys. Rev. A **63**, 012710 (2000).
[11] J. Mitroy and M. W. J. Bromley, Phys. Rev. A **68**, 052714 (2003).
[12] D. E. Johnson and J. G. Eden, J. Opt. Soc. Am. B **2**, 721 (1985).
[13] O. Allard, S. Falke, A. Pashov, O. Dulieu, H. Knöckel, and E. Tiemann, Eur. Phys. J. D **35**, 483 (2005).